ORIGINAL PAPER

Nonlinear dynamics of a rotor–stator system with contacts

Alberto Paiva · Rodrigo Veronese Moreira · Alex Brandão · Marcelo A. Savi

Abstract Rotating system dynamics are usually related to the contact between rotor and stator, which induces undesirable behaviors that may both compromise endurance and prevent the system from working properly. In this regard, aiming a better understanding of this kind of occurrence, this work deals with the nonlinear dynamics of a Jeffcott-based rotor–stator system modeled as a four-degree of freedom sketch enabling nonsmooth impact between them. The contact between rotor and stator involves both normal impact and tangential rubbing. Based on the contact between rotor and stator, three kinds of motion are classified: no contact, intermittent contact and full contact. Numerical simulations are carried out mapping dynamical patterns and defining different kinds of motion. A parametric analysis is developed and results comprise parameter spaces varying three main physical quantities: rotating speed, contact stiffness and friction coefficient.

Keywords Jeffcott rotor · Rotordynamics · Nonsmooth system · Rubbing · Nonlinear dynamics · Chaos

A. Paiva
Volta Redonda School of Engineering, Universidade Federal Fluminense, 420 Trabalhadores Av., Volta Redonda, RJ 27.255-250, Brazil
e-mail: albertopaiva@id.uff.br

R. V. Moreira
NVH Department, MAN Trucks and Buses SE, 8005 Renato Monteiro St., Porto Real, RJ 27.570-000, Brazil
e-mail: rveronese@id.uff.br

A. Brandão · M. A. Savi (✉)
COPPE - Department of Mechanical Engineering Center for Nonlinear Mechanics (Mecanon), Universidade Federal Do Rio de Janeiro, Rio de Janeiro, RJ 21.941.972, Brazil
e-mail: savi@mecanica.coppe.ufrj.br

A. Brandão
e-mail: alexbrandao@mecanica.coppe.ufrj.br

1 Introduction

Rotating machines have been used in large scale since the first industrial revolution. Accordingly, for more than a 100 years, dynamical models have been developed and refined in order to describe such system behavior. Rotating systems may have complex assembling characteristics, involving multiple components; however, unfailingly, three of them are essential: the rotor that accounts for the system rotational inertia; the shaft that supports the rotor; and the supporting bearings. The dynamical analysis of this kind of system is not an easy task, not only due to intrinsic effects such as asymmetry, unbalance, clearances, among others, but also for components interaction, especially impact and friction.

The first attempts toward rotordynamics modeling took place in the late nineteenth century with Rankine in 1869, followed by some other contributions by De Laval, Dunkerley and Föppl. In the beginning of the twentieth century, Jeffcott proposed a simple planar model, consisting of a symmetric rotor mounted on a uniform shaft with equal distance from identical bearings, with two decoupled degrees of freedom (DOF). Despite its simplicity, the Jeffcott model became very useful and is still employed in rotordynamics analyses. Since then, other complex effects have been incorporated into these precursor models by several authors, as reported in different classical books [24, 28], 21, 37]. In fact, new relevant scientific contributions are identified in the literature after computer evolution since the last quarter of the twentieth century. Ahmad [1] elaborated a review work concerning rotor–stator contact features. Besides providing plentiful references on the subject, the author discussed the following topics: frequency rotation influence, friction effect, whirl occurrence, different support stiffness, pre-loading importance, torsional behavior, thermal problems, among others.

Concerning studies involving contact between rotor and stator, there are numerous relevant works in the literature. Choy and Padovan [12] developed one of the pioneer works investigating rubbing effect over a Jeffcott rotor system nonlinear dynamics. By means of parametric analyses varying unbalance, stiffness, damping and friction coefficient, they investigated rotor orbits during successive rubs. Muszynska and Goldman [29] conducted a numerical–experimental study concerning the same previous mechanical system. Both results were in agreement attesting that higher damping values inhibit chaotic behaviors. Popprath and Ecker [31] incorporated the stator inertia into the original Jeffcott rotor–stator model and formulated a model considering contact stiffness, damping and friction. They carried out numerical simulations investigating the system dynamical response, through Poincare maps and bifurcation diagrams, while varying parameters such as rotating speed, stator inertia and stator supports damping. They suggested that lower stator supports damping values increase the system dynamical behavior complexity.

Chavez and Wiercigroch [10] conducted an analytical–numerical study focused on grazing phenomena in a nonsmooth Jeffcott rotor system. The authors adopted the path-following method, instead of time integration over large intervals. Along results, they distinguished contact from non-contact situations, while varying the rotation frequency. Besides that, they also identified stable and unstable regions in the frequency domain, attesting their periodicity or even chaotic behavior. Brandão et al. [7] investigated the nonlinear dynamics of a nonsmooth Jeffcott rotor–stator system subjected to impact and rubbing. The authors explored different dynamical patterns through bifurcation diagrams varying the rotation speed. Mokhtar et al. [26] discarded the rubbing effect in the formulation of a Jeffcott rotor–stator system and compared their achievement with previous results from the literature, which considered pure rubbing. Their numerical results comprised frequency spectra and closed orbits of the rotor geometrical center, demonstrating that pure sticking and pure rubbing provide similar results, despite of some quantitative discrepancy.

Behzad and Alvandi [5] numerically explored the rubbing effect of a Jeffcott rotor against a segmented stator due to unbalance, in order to mitigate clearances. The authors treated exclusively forward rubbing behaviors, while passing through critical rotation speed. Two main parameters were varied: the number of stator segments and their respective stiffness. Results are able to capture some typical phenomena, such as resonance speed, jump phenomena and chaotic motion. Moreira and Paiva [27] exploited the numerical response of friction influence over the nonlinear dynamics of a Jeffcott rotor–stator that may undergo contact. Their results included a space parameter analysis involving rotating speed and contact stiffness to classify the contact nature (intermittent/permanent) and bifurcation diagrams varying friction coefficient. As a conclusion, they pointed out critical range values of these parameters that propitiate more complex behaviors such chaos.

Chipato et al. [11] dealt with the friction influence over rotor–stator nonlinear contact dynamics. They incorporated a smoothed hyperbolic tangent friction function into a 2-DOF model describing a rotor supported by a cantilever shaft. Bifurcation diagrams sweeping rotation frequency for different values of friction coefficient and eccentricity are presented together with trajectories of the rotor geometrical center, frequency spectra and spectral intensity maps. Results characterized two types of bouncing solutions, depending on friction level: asynchronous periodic

bouncing and synchronization of frequency components. Yang et al. [43] numerically investigated the influence of different coating stiffness on the dynamical response of a Jeffcott rotor subjected to rub-impact forces. They used the Hertz model for impact together with an interpolation method to evaluate the contact stiffness. Their results suggested that a softer coating stiffness may present simpler (periodic) dynamical responses, compared to a harder coating (chaotic) one.

Some other authors explored the unbalance in rotor-alone systems, without considering contact with other parts. Yao et al. [44] performed a numerical–experimental investigation of the unbalance parameters influence over the rotor dynamical response. Their approach was based on a modal expansion methodology combined with an optimization procedure that enabled to identify the axial location of the unbalance, its magnitude and phase. The analyses consider trajectories of the rotor geometrical center in the state space and frequency spectra. Tuckmantel and Cavalca [38] established a comparison between two approaches for modeling forces and moments generated by disc coupling under angular misalignment. The system consisted of two shafts—each of them supported by two journal bearings with a single rotor—connected by a disc coupling. Each approach displayed orbits described by the neutral line in some discrete points of both axes, in contrast with a reference orbit for an aligned axes condition, for several rotation speeds.

Another possibility of contact in rotating machines is between shaft and bearings, which may be a journal bearing, a ball or roller bearing or even a magnetic bearing, with different geometries and different lubricating/contact conditions. Several authors dedicated their effort toward this branch of knowledge. Chavez et al. [9] studied a Jeffcott rotor subjected to impact against a snubber ring with anisotropic support. The authors adopted a rigorous derivation for the contact forces, aiming a more realistic behavior to better fit experimental results. They compared numerical and experimental results, using bifurcation diagrams and some periodic orbits in displacement state subspaces, achieving a very good agreement between them.

Varney and Green [39] explored the nonlinear dynamics of an asymmetrically supported rotor–stator undergoing contact. The authors considered different stiffness values for each planar direction, besides a

coupling stiffness between both directions. They scrutinized the influence of support asymmetry level on the nonlinear rotor response, using orbits/trajectories paths of the rotor geometrical center, frequency spectra and bifurcation diagrams. Afterward, Ali Hajnayeb and Sedighi [3] identified some inconsistency in the original formulation of Varney and Green [39], rebuilding some of the original results and attesting changes in the rotor dynamical responses.

Boyaci [6] investigated the dynamical stability of a Jeffcot rotor supported by semi-floating ring bearings with inner and outer oil film, by means of bifurcation diagrams and parameters space involving the unbalance load and the rotor speed. Different types of bifurcation are presented, characterizing specific behaviors as a function of rotation frequency such as stable/unstable, synchronous/subsynchronous, critical limit cycle, among others.

Saint Martin et al. [33] developed an analytical–numerical study concerning model reduction for a rotor alone without contact. They revisited three reduction methods present in the literature, with some refinement incorporated to one of them. The modified method was applied to two rotors examples with different inertial gyroscopic effects, originally modeled with a large number of DOFs. Numerical results provided good agreement between reduced and complete model responses, considering frequency response functions and Campbell diagrams. Chasalevris [8] studied the bifurcation features and the stability threshold of a Jeffcott rotor supported by two bearing types. Sophisticated bearings models included the foundation properties of their pedestals. The author focused on both classifying the type of bifurcation—subcritical or supercritical—and identifying the stability of limit cycles. He concluded that subcritical bifurcation can be more harmful in practical applications since the system may lose stability in rotating speeds lower than the threshold speed of instability.

Wang [41] conducted a numerical analysis of the fit looseness fault between outer ring and housing due to lubrication film squeezing in a Jeffcott rotor. The target was to verify the SFD (squeeze film damper) capacity as a passive vibration reduction method. As a conclusion, the author discussed details of the system response near critical speed and their harmonics for different contact situations (continuous *versus* discontinuous). El-Sayed and Sayed [16] studied a flexible Jeffcott rotor supported by two identical nonlinear

bearings to investigate the system response. The authors numerically investigated how the stiffness and the applied load affect both the Hopf bifurcation stability and the associated limit cycle.

Still regarding rotating system supports, a more recent solution lies upon the use of smart materials (such as shape memory alloy or magneto-rheological fluid) to inhibit undesired behaviors. In this regard, [19, 20] conducted a numerical–experimental work embedding shape memory alloy (SMA) springs to support usual ball bearings. Their idea was to tune up the SMA stiffness through an active temperature control to avoid resonance problems, while passing by the critical speed. Experimental results attested the feasibility of the original proposal. Silva et al. [35] numerically investigated the nonlinear dynamics of a Jeffcott rotor undergoing nonsmooth impact against a stator supported by SMA restoring elements. Alves et al. [4] performed a numerical–experimental dynamical analysis of a rotor-bearing test rig suspended by shape memory alloy wires. Their results show that higher vibration amplitudes and higher SMA temperature provides higher damping effect of the SMA elements. Srinivas et al. [36] presented a state-of-the-art review of active magnetic bearings applied to rotordynamics systems. Rahman et al. [32] scrutinized the synchronous *versus* asynchronous whirling response of a Jeffcott rotor supported by a pseudoelastic SMA shaft. Their results revealed that SMA shaft caused resonance at a lower rotation speed compared to that provided by the linear elastic shaft.

Another interesting analysis consists of including the shaft torsion as a third DOF. Edwards et al. [14] incorporated a new equation of motion for rotation into the previous Jeffcott rotor formulation and discussed resonant conditions by means of bifurcation diagrams, varying the forcing frequency and the torsional stiffness. Al-Bedoor [2] formulated a coupled model considering torsional and lateral vibrations for a rotor–stator system undergoing rubbing effect. The coupled model provided more complex rotor dynamical responses compared with the original Jeffcott model with only lateral vibration. Vlajic et al. [40] also considered both torsional and lateral effects in a rotor–stator system, subjected to impact. Firstly, the authors discussed forward and backward whirling conditions, besides that, they explored parameter spaces involving the rotor angular frequency and the friction coefficient to characterize the

contact nature. Three situations are observed, classified into no contact, pure stick and stick–slip.

The torsional response of flexible shafts is of special interest for drill-string applications, for instance, during torsional stick–slip phenomenon due to bit-rock interaction, especially in non-vertical wells. Kapitaniak et al. [23] conducted a numerical–experimental study concerning the rotordynamics of a coupled drill-string model exposed to contact. They experimentally evaluated a parameters space involving weight on bit and rotation speed to distinguish chaotic responses from periodic ones. Besides that, they characterized whether the whirling is forward or backward. Finally, they numerically investigated the initial conditions influence over the system dynamical response, classifying into periodic forward, periodic backward and chaotic forward whirl. Xie et al. [42] conducted the modeling and numerical simulation of a drill-string for a horizontal well, comprising two rotating inertias. The model included: longitudinal, lateral and torsional vibrations, intermittent contact of the drill-pipe with the borehole wall and a special modeling of the cutting process to couple the axial and torsional motions. The analyses were based upon orbits/trajectories in displacement state subspaces, focused on varying the rotation speed and the dynamic friction coefficient. Nguyen et al. [30] studied the nonlinear dynamics of a drill-string applied to curved wells. They used a specific reduction model technique, considering the well curvature and its implications to model the interaction between the drill-string and the bottom hole through finite element method. Results identified bit-bounce and stick–slip occurrences.

Regarding experimental analyses, researchers explored different contact phenomena related to whirling, torsional (stick–slip) or axial (bit-bounce) motion. Lahriri and Santos [22] developed an analytical–numerical–experimental study involving the nonlinear dynamics of rotor system with bearing impact against housing. Results compared numerical and experimental results, by means of trajectories of the rotor geometrical center, time evolution for different quantities and waterfall FFT spectra. They concluded that numerical results overestimated the contact forces values, while compared to experimental results.

Fonseca et al. [17] developed a numerical–experimental study of a rotor system considering a backup bearing, consisting of radial pins responsible for constraining excessive vibration amplitudes of the

shaft. They analyzed numerical and experimental responses for orbits/trajectories paths of the rotor geometrical center, for different input torque conditions, with and without impact against the constraining pins. Ehehalt et al. [15] provided a review of previous experimental studies aiming to compile and discuss several rotor–stator contact behaviors, such as synchronous motions, forward/backward whirl, sub/superharmonic motions, chaos, considering different assembling configurations. Once again, results were focused on orbits/trajectories of the rotor geometrical center and frequency spectra. Fonseca et al. [18] presented a theoretical–experimental study, comparing the rotor response while supported by two different backup bearings: a pinned and a ball bearing. They presented orbits/trajectories of the geometrical rotor center for both cases and concluded that the pinned bearing provided a more effective backup constraint.

Zhang et al. [45] conducted a numerical–experimental study of the coupling effects between looseness and a cubic nonlinear supporting stiffness for a two-disc rotor. Numerical simulations involved bifurcation diagrams, time histories, frequency spectra, phase portraits and Poincaré maps. At last, the authors proposed an experimental test rig to verify the main numerical conclusions about the dynamical response for different rotation speed ranges.

The present work focuses on a multiparametric numerical analysis of a Jeffcott rotor surrounded by a stator, undergoing nonsmooth impact. The system consists of a four-degree of freedom, corresponding to planar displacements of each part—rotor and stator. The stator inner surface is subjected to contact, being coated with a wear layer, which may undergo an elastic restitution (normal direction) and Coulomb friction (tangential direction). Numerical simulations are carried out and results consider steady-state responses, discarding the transient regimes. Dynamical pattern identification is based upon the evaluation of the converged values of the Lyapunov exponents. Besides that, a brute force algorithm is developed to classify selected periodicities, by real time monitoring of the state variable time evolution. Parametric analysis is developed showing parameter spaces varying three quantities: rotating speed, contact stiffness and friction coefficient. Initially, the maps classify the rotor–stator contact nature into no contact, intermittent contact or full contact; then, new maps classify the dynamical patterns into different

periodicities and chaotic/hyperchaotic motions. Nonlinear tools as bifurcation diagrams, Lyapunov exponents, Poincaré sections and orbits/trajectories in state subspaces provide a proper comprehension of the map results.

2 Mathematical model

This section is devoted to the formulation of the dynamical equations of motion for the rotor–stator system. Rotordynamics is related to several complex phenomena such as gyroscopic effects, shaft torsional vibration or sub/superharmonics resonance. Multiple degrees of freedom are needed to encompass all these aspects, which usually employs finite element analysis. Reduced-order models are interesting to describe the essential aspects of the rotordynamics, including critical behaviors promoted by the system unbalance and the contact between rotor and stator. Complex behaviors are expected due to nonsmooth nonlinearities, including chaos.

In this regard, a four-degrees of freedom nonsmooth Jeffcott rotor, being two associated with the rotor and two related to the stator, is of concern to represent the rotordynamical system. The rotor–stator physical model is presented in Fig. 1, where the rotor has mass m_r and rotating speed Ω, which center of mass (point G) has an eccentricity e from its geometric
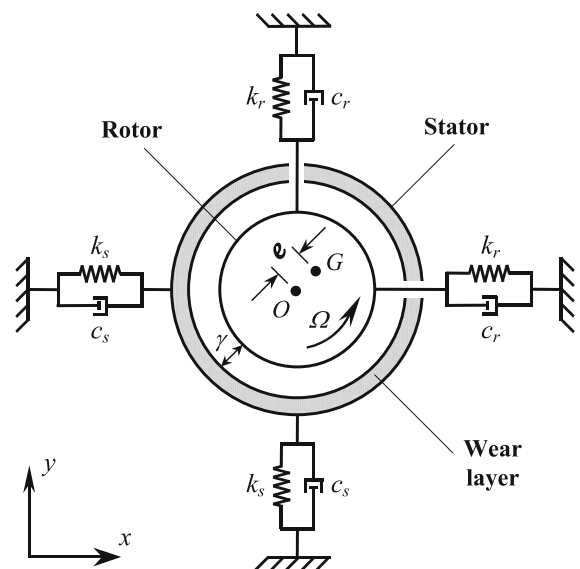

Fig. 1 Rotor–stator physical model

center (point O), due to unbalance. The stator with mass m_s encloses the rotor with a constant radial gap γ, measured in a rest position of rotor and stator, considering their respective weight forces. Both rotor and stator have linear supports with respective equivalent stiffness and damping k_r, c_r and k_s, c_s. The inner surface of the stator is coated with an elastic wear layer, which may undergo impact and friction with the rotor, with stiffness k_C and friction coefficient μ. Concerning the contact hypotheses, the following assumptions are adopted: The rotating motion of the stator is neglected; the contact between the rotor and the stator is assumed to be punctual, rather than a surface contact and therefore, the wear layer undergoes only normal radial strain.

Figure 2 presents a disturbed condition for the rotor–stator system, aiming the model kinematical analysis. Note that points O_r and O_s denote the disturbed position of rotor and stator geometric centers, respectively; vectors $\underline{r}_r$ and $\underline{r}_s$ represent the absolute position of points O_r and O_s, with respect to the original geometric center rest position (point O); the vector $\underline{r}_{sr}$ concerns the relative displacement between rotor and stator; α is the angle between the vector $\underline{r}_{sr}$ and the inertial x axis, measured anticlockwise; x_r and y_r are the planar rotor displacement components of $\underline{r}_r$ in x and y directions, respectively; analogously, x_s and y_s the planar stator displacement

components of $\underline{r}_s$ and x_{sr} and y_{sr} are the relative displacement components of $\underline{r}_{sr}$. Some useful geometrical relations are given in Eq. (1).

$$
\begin{aligned}
&|\underline{r}_{sr}| = \sqrt{(x_r - x_s)^2 + (y_r - y_s)^2} \\
&x_{sr} = x_r - x_s = |\underline{r}_{sr}| \cos \alpha \Rightarrow \cos \alpha = \frac{x_r - x_s}{|\underline{r}_{sr}|} \\
&y_{sr} = y_r - y_s = |\underline{r}_{sr}| \sin \alpha \Rightarrow \sin \alpha = \frac{y_r - y_s}{|\underline{r}_{sr}|}
\end{aligned}
\tag{1}
$$

The contact occurs when the modulus of the relative displacement between rotor and stator $|\underline{r}_{sr}|$ exceeds the gap γ. Hence, if $|\underline{r}_{sr}| < \gamma$, the system operates on no contact mode. If $|\underline{r}_{sr}| \geq \gamma$, the contact takes place. It is worthwhile to notice that, when there is no contact, the system behaves like two independent 2-DOF linear systems, with the rotor subjected to a forcing excitation.

Kinetic analysis is now of concern considering the free-body diagram for the rotor and for the stator, presented in Fig. 3. F_{r_x} and F_{r_y} are the rotor support reaction forces in the x and y directions, respectively; analogously, F_{s_x} and F_{s_y} are the stator support reactions forces; F_{C_n} and F_{C_t} are the normal and tangential components of the contact force; F_{G_x} and F_{G_y} are the centrifugal force components in the x and y directions, respectively. Finally, P_r and P_s are the
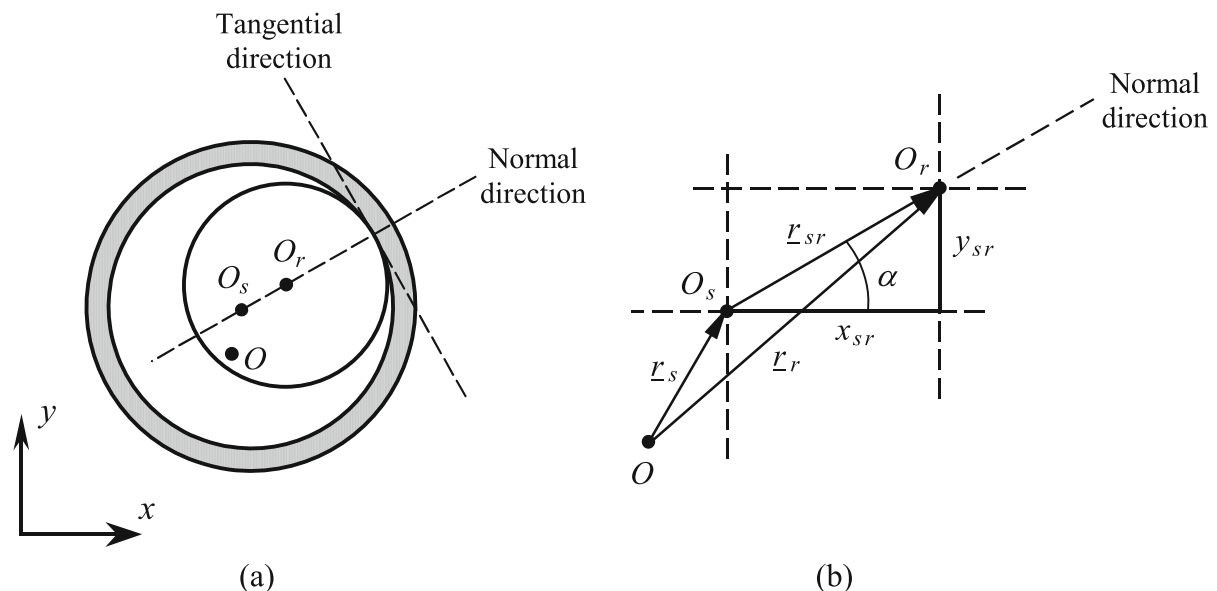

Fig. 2 Disturbed condition for the rotor–stator system. **a** Physical sketch; **b** detail of vector representation
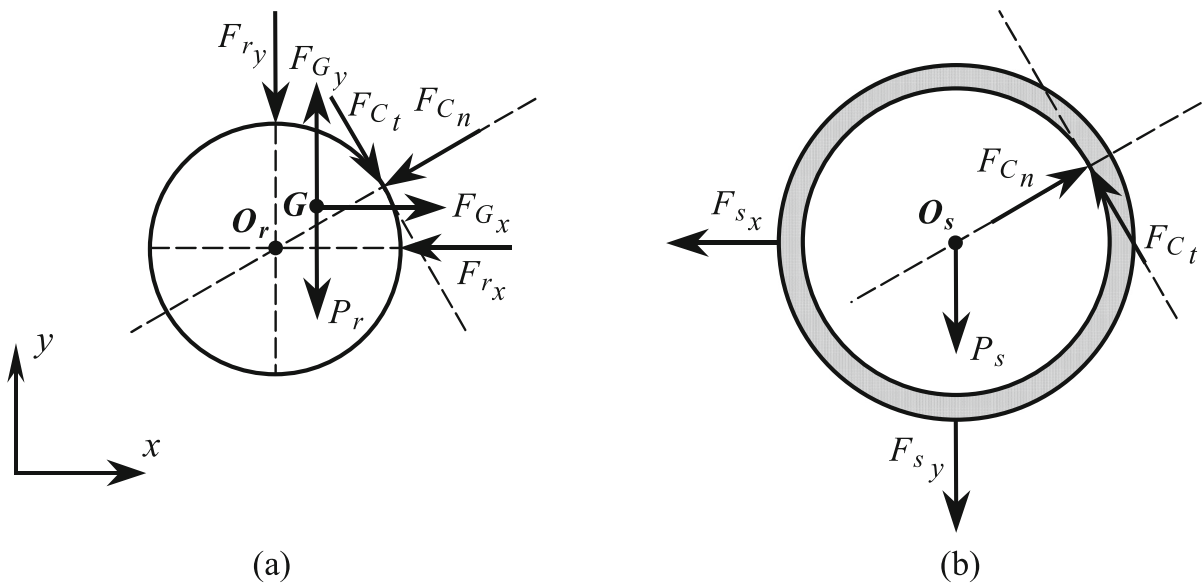
Fig. 3 Rotor free-body diagram for: **a** rotor and **b** stator

rotor and stator weight forces, respectively, while g is the acceleration due to gravity.

In order to incorporate the contact force into the equations of motion, the normal and tangential components F_{C_n} and F_{C_t} acting upon rotor should be decomposed in the x and y directions (F_{C_x} and F_{C_y}, respectively), as follows:

$$F_{C_x} = -F_{C_n} \cos \alpha + F_{C_t} \sin \alpha \text{ and}$$
$$F_{C_y} = -F_{C_n} \sin \alpha - F_{C_t} \cos \alpha \qquad (2)$$

By applying the Newton's second law for both x and y directions, the following equations of motion for both the rotor and the stator are obtained:

$$
\text{Rotor}: \begin{cases} -F_{r_x} + F_{G_x} + F_{C_x} = m_r \ddot{x}_r \\ -F_{r_y} + F_{G_y} + F_{C_y} - P_r = m_r \ddot{y}_r \end{cases}
$$
$$
\text{Stator}: \begin{cases} -F_{s_x} - F_{C_x} = m_s \ddot{x}_s \\ -F_{s_y} - F_{C_y} - P_s = m_s \ddot{y}_s \end{cases}
\qquad (3)
$$

where $(\bullet)$ denotes the time derivative $(\bullet) = d(\ )/dt$.

The rotor and stator reaction forces components are given by:

$$\text{Rotor}: F_{r_x} = c_r \dot{x}_r + k_r x_r \text{ and } F_{r_y} = c_r \dot{y}_r + k_r y_r$$
$$\text{Stator}: F_{s_x} = c_s \dot{x}_s + k_s x_s \text{ and } F_{s_y} = c_s \dot{y}_s + k_s y_s$$
$$(4)$$

The centrifugal force components in the x and y directions are given by:

$$F_{G_x} = m_r e \, \Omega^2 \cos (\Omega t + \phi) \text{ and}$$
$$F_{G_y} = m_r e \, \Omega^2 \sin (\Omega t + \phi) \qquad (5)$$

where φ is the initial phase angle, defining the angular position of the center of mass (point G) at $t = 0$ s, measured anti-clockwise from the inertial x axis.

Recalling that the normal component F_{C_n} results from coating wear layer indentation, given by $\delta = (|\underline{r}_{sr}| - \gamma)$; and the tangential component F_{C_t} arises from friction between rotor and stator, these components of the contact force are, respectively, given by:

$$F_{C_n} = k_C \, \delta = k_C \, (|\underline{r}_{sr}| - \gamma)$$
$$F_{C_t} = \text{sign}(v_t) \, \mu \, F_{C_n} = \text{sign}(v_t) \, \mu \, k_C \, (|\underline{r}_{sr}| - \gamma)$$
$$(6)$$

where $\text{sign}(v_t) = \begin{cases} -1 & \text{if } v_t < 0 \\ 0 & \text{if } v_t = 0 \\ 1 & \text{if } v_t > 0 \end{cases}$ and v_t is the total

tangential velocity component at the contact point, given by:

$$v_t = \Omega R_r - \dot{x}_{sr} \sin \alpha + \dot{y}_{sr} \cos \alpha \qquad (7)$$

Since R_r is the rotor radius, the term ΩR_r represents the tangential velocity component of a point located at

the rotor surface due to spin velocity Ω while the two last remaining terms correspond to the tangential component of the relative velocity between rotor and stator. As a matter of fact, these terms evaluate whether the rotor precession angular velocity ($\dot{\alpha}$) is backward ($v_t < 0$) or forward ($v_t > 0$). The quantities $\dot{x}_{sr}$ and $\dot{y}_{sr}$ may be obtained through either analytical derivation of Eqs. (1) for x_{sr} and y_{sr} or numerical estimation. The function $\text{sign}(v_t)$ defines the direction of the tangential contact force component F_{C_t}.

Combining Eqs. (1), (2) and (6), it is possible to obtain the components F_{C_x} and F_{C_y} of the contact forces:

$$F_{C_x} = \begin{cases} 0 & \text{if } |\underline{r}_{sr}| < \gamma \\ k_C \left(|\underline{r}_{sr}| - \gamma \right) \dfrac{1}{|\underline{r}_{sr}|} \left[-(x_r - x_s) + \text{sign}(v_t)\,\mu\,(y_r - y_s) \right] & \text{if } |\underline{r}_{sr}| \geq \gamma \end{cases}$$
$$F_{C_y} = \begin{cases} 0 & \text{if } |\underline{r}_{sr}| < \gamma \\ k_C \left(|\underline{r}_{sr}| - \gamma \right) \dfrac{1}{|\underline{r}_{sr}|} \left[-(y_r - y_s) - \text{sign}(v_t)\,\mu\,(x_r - x_s) \right] & \text{if } |\underline{r}_{sr}| \geq \gamma \end{cases}$$

(8)

[25, 34]. Divenyi et al. [13] employed a numerical procedure where transition regions are defined to govern the dynamical response during the transition from one set of equations to another. Savi et al. [34] employed the same method and provided an experimental verification of the procedure. Therefore, each subspace and each transition region have its own ordinary differential equations set, smoothening the system dynamics. Alternatively, variable time steps can be employed to integrate these governing equations. One possible solution for the time step definition is based on the seek to the transition exact moment. The other possibility is to establish a comparison

Under these assumptions, all forces are evaluated allowing to write the equations of motion in their final form:

$$m_r \ddot{x}_r + c_r \dot{x}_r + k_r xE = m_r e\Omega^2 \cos(\Omega t + \phi) + F_{C_x}$$
$$m_r \ddot{y}_r + c_r \dot{y}_r + k_r y_r = m_r e\Omega^2 \sin(\Omega t + \phi) + F_{C_y} - m_r g$$
$$m_s \ddot{x}_s + c_s \dot{x}_s + k_s x_s = -F_{C_x}$$
$$m_s \ddot{y}_s + c_s \dot{y}_s + k_s y_s = -F_{C_y} - m_s g$$

(9)

where the coupling contact forces F_{C_x} and F_{C_y} are defined according to Eq. (8).

3 Numerical simulations

Nonsmooth systems have a complex behavior and their description is related to many mathematical and numerical difficulties. In brief, they can be understood as a finite number of continuous subspaces where each subspace is governed by a set of differential equations, which characterizes the general governing equations as a switch model. These assumptions motivate the description of nonsmooth systems by smoothed forms

between methods with different integration orders, defining a proper time step based on a prescribed tolerance.

Although these procedures allow one to use larger time steps, a proper choice of a constant time step from a convergence analysis can be employed to perform numerical simulations. This section presents results obtained through numerical simulations using the fourth-order Runge–Kutta method considering constant time steps smaller than $2\pi/1000\Omega$ defined from a convergence analysis. In essence, time steps are defined by establishing a comparison with variable time steps (MATLAB ODE-45 with tolerance of 10^{-8}). The choice of this integrator aims to minimize possible inaccuracies during the contact transition and

Table 1 Rotor–stator system parameters

m_r (kg)	k_r (N/m)	c_r (Ns/m)	e (m)	φ (rad)
50	980×10^3	280	0.001	0
m_s (kg)	k_s (N/m)	c_s (Ns/m)	γ (mm)	
50	$14{,}580 \times 10^3$	2700	6	

at the same time, allows the use of some nonlinear tools employed in this analysis.

Initially, the contact nature is mapped by means of basins of attraction (parameter spaces), varying three main system parameters: rotating speed, Ω; contact stiffness, k_C; and friction coefficient, μ. Three conditions are identified: no contact, intermittent contact and full contact, associated with a full annular contact. The dynamical response complexity of both rotor and stator is investigated through bifurcation diagrams, Lyapunov exponents and new basins mapping the

dynamical pattern (periodic, chaotic, hyperchaotic) in parameter space.

Table 1 presents the rotor–stator system parameters used throughout the simulations, except for those that are varied: Ω, k_C and μ. All initial conditions are considered null, unless for rotor and stator displacements in the y-direction that correspond to the vertical static deflection, due to their weight forces.

Parametric analysis starts by considering a basin of attraction associated with a space composed by contact stiffness *versus* rotating speed. Figure 4
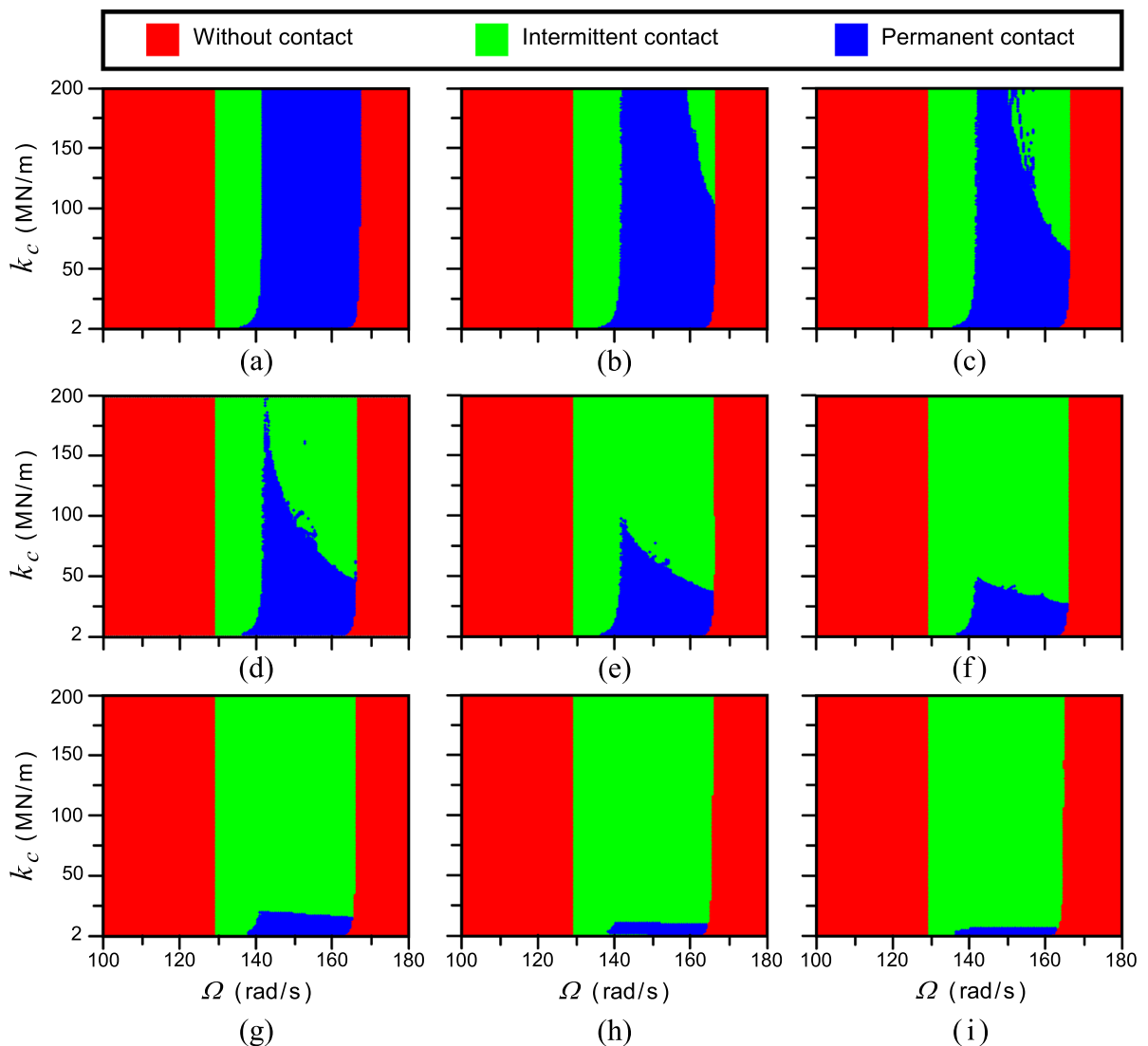
Fig. 4 Basin of attraction mapping the contact nature evolution varying the friction coefficient. **a** $\mu = 0$; **b** $\mu = 0.095$; **c** $\mu = 0.100$; **d** $\mu = 0.105$; **e** $\mu = 0.110$; **f** $\mu = 0.120$; **g** $\mu = 0.150$; **h** $\mu = 0.200$; **i** $\mu = 0.300$

presents the evolution of this basin of attraction varying the friction coefficient. All basins reveal non-contact regions for low ($\Omega < 130$ rad/s) and high ($\Omega > 170$ rad/s) rotating speed values, regardless of both contact stiffness and friction coefficient values. Within an intermediate range of rotating speed values (130 rad/s $< \Omega <$ 170 rad/s), intermittent contact and full contact conditions coexists. Observing this range during the basin of attraction evolution according to friction coefficient increase, the full contact region undergoes erosion and shrinks, at the expense of the intermittent contact region enlargement, standing only for very low values of the contact stiffness. It should be highlighted that the linearized natural frequency for the rotor alone is given by: $k_r/m_r = 140$ rad / s. Note that the vertical bound separating the intermittent contact region from the full contact one relies around this value. Therefore, it is expected to obtain interesting results close to this rotating speed value.

The richest dynamical behavior should take place for an intermittent contact condition; therefore, it is possible to infer that higher friction coefficient values should increase the system dynamics complexity. Besides that, for low contact stiffness values, a complexity loss is expected, regardless of the friction coefficient value. These trends are deeper discussed in the sequel.

The analysis of the influence of the friction coefficient over the basin of attraction erosion is now of concern. Figure 5a illustrates how the permanent contact region shrinks, such that the contour lines indicate the boundaries for different friction coefficients, according to the basins of Fig. 4. The introduction of the friction coefficient nucleates an intermittent contact region near the right upper bound, within the range of interest (130 rad/s $< \Omega <$ 165 rad/s) of the parameter space. As the friction coefficient increases, it grows left and downwards. Figure 5b shows vertical (varying k_C) and horizontal (varying Ω) routes for further bifurcation analyses for the specific case of $\mu = 0.1$. Besides that, the dynamical behavior of the intersection point between these routes ($k_C = 100$MN/m; $\Omega = 130$ rad/s and $\mu = 0.1$) is investigated by means of orbits/trajectories and Poincare sections in state subspaces.

Figure 6 presents the system response of both parts—rotor and stator—as well as for the system as whole. Figure 6a and b show the physical trajectories for the rotor and for the stator, in the state subspaces $x_r \times y_r$ and $x_s \times y_s$, respectively. For the rotor (Fig. 6a), a closed orbit can be identified, indicating periodic behavior, while the respective Poincare section displays a single point, attesting a period-1 behavior. For the stator (Fig. 6b), tangle trajectories associated with a more complex behavior are obtained, together with a dense cloud of points in the Poincare section, characterizing a strange attractor related to the stator chaotic behavior, which is confirmed through
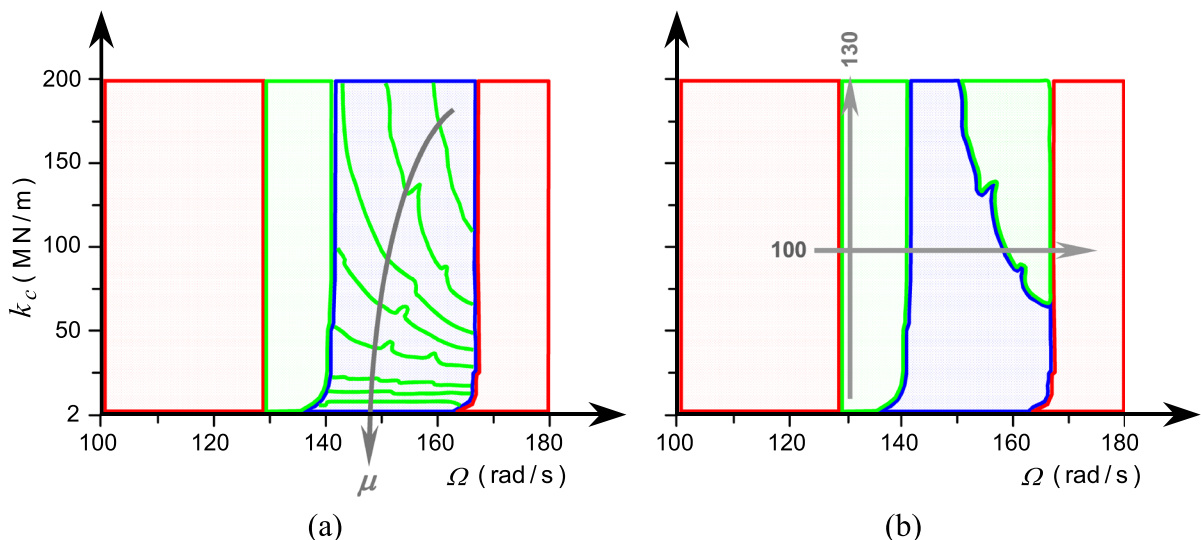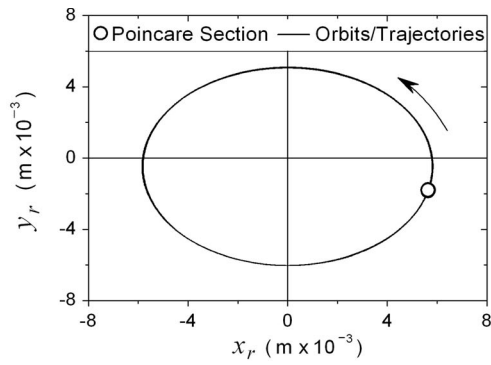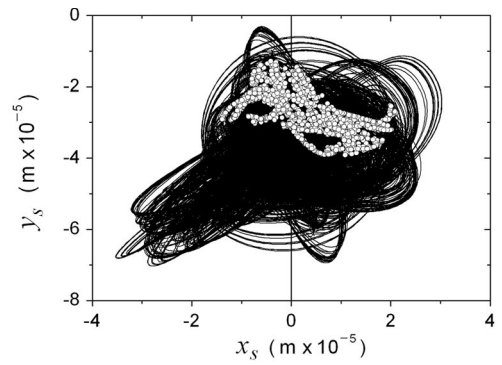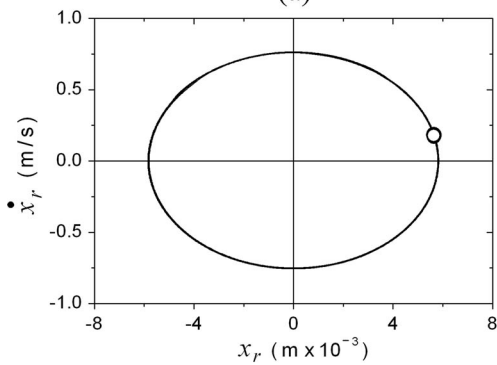

Fig. 5 Bifurcation analysis based on the basin of attractions. **a** Friction coefficient influence over the basin of attraction erosion; **b** Routes for bifurcation diagrams analysis for $\mu = 0.1$;
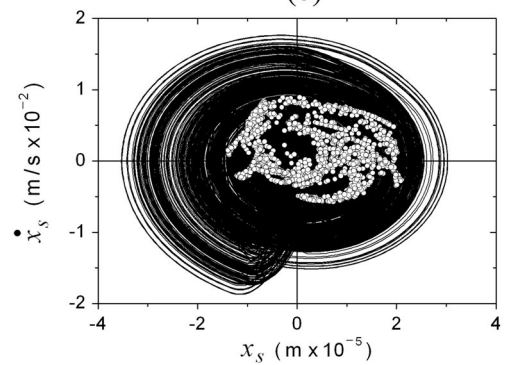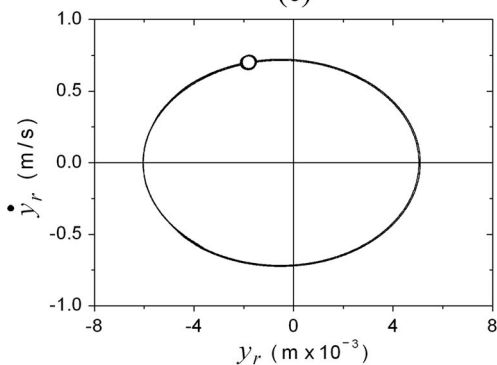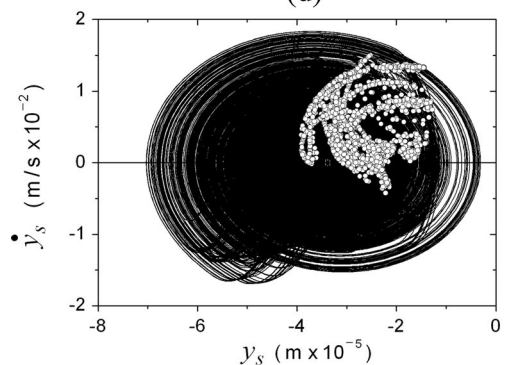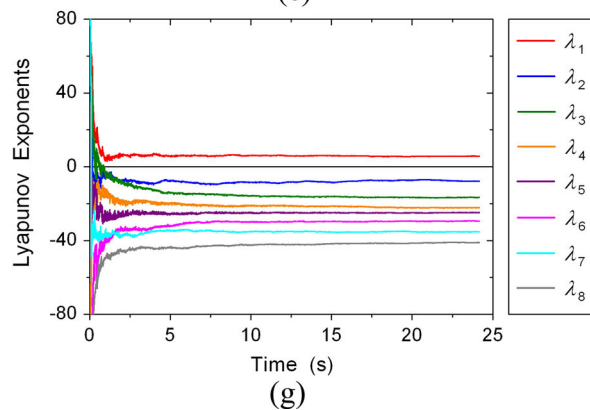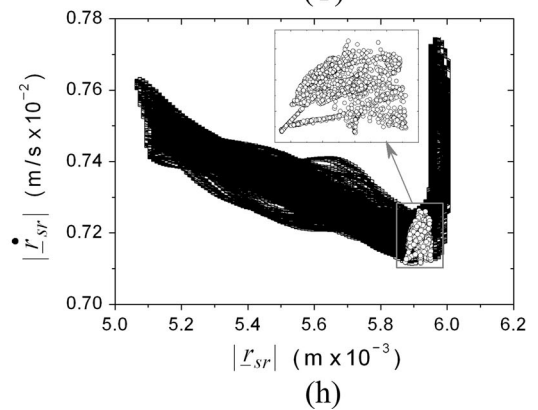
(a)

(b)

(c)

(d)

(e)

(f)

(g)

(h)

◄ **Fig. 6** Rotor and stator dynamical analysis with fixed $\mu = 0.1$; $k_C = 100$ MN/m; $\Omega = 130$ rad/s. **a** and **b** Physical trajectories with Poincare sections; **c**, **d**, **e** and **f** Trajectories and Poincare sections for x and y directions for the rotor and the stator, respectively; **g** Lyapunov exponents' spectrum; **h** Trajectories in the state subspace $|\underline{r}_{sr}| \times |\underline{\dot{r}}_{sr}|$

the Lyapunov exponents' spectrum (Fig. 6g), presenting one positive exponent, where: λ_i ($i = 1, 2, 3, ..., 8$) holds for x_r, $\dot{x}_r$, y_r, $\dot{y}_r$, x_s, $\dot{x}_s$, y_s and $\dot{y}_s$, respectively. Figure 6c, d shows the orbits with the respective Poincare sections for the rotor and for the stator subspaces $x_r \times \dot{x}_r$ and $x_s \times \dot{x}_s$, related to the x-direction, while Fig. 6e, f show analogous results for the y-direction ($y_r \times \dot{y}_r$ and $y_s \times \dot{y}_s$ subspaces, respectively). In both directions, it is possible to identify period-1 responses for the rotor and, again, a cloud of points for the stator with a typical chaotic lamellar structure. Finally, Fig. 6h shows the trajectories and the strange attractor in the state subspace considering the relative displacement modulus between rotor and stator $|\underline{r}_{sr}|$ and its derivative. This result provides a more accurate impression about the system dynamics as a whole, since $\underline{r}_{sr}$ involves x_r, y_r, x_s and y_s, according to Eq. (1). It is interesting to notice that the system as a whole incorporates the most complex dynamical pattern between rotor and stator, which means that the system follows the stator dynamics.

This analysis enables two conclusions: Both rotor and stator present the same qualitative dynamical behavior for both x and y directions; and the stator has a richer (chaotic) dynamical behavior, while compared to the rotor (period-1). For these two reasons, from this point on, only the x-direction of the stator is investigated.

Bifurcation diagrams are built from a stroboscopically sampled state variable under the slow quasi-static increase in a system parameter. A brute force method is employed and therefore, only stable branches are observed. On this basis, bifurcation diagrams provide a global picture of the system dynamics, illustrating qualitative changes on system responses. Since unstable branches are not evaluated, bifurcations are not classified. Figure 7 shows bifurcation diagrams following both routes presented in Fig. 5(b), for $\mu = 0.1$. Figure 7a shows the diagram sweeping the contact stiffness parameter k_C for a fixed

value of the rotating speed ($\Omega = 130$ rad/s), superposed upon the converged values of the Lyapunov exponents' spectra. Figure 7b displays the bifurcation diagram sweeping the rotating speed parameter Ω for a fixed value of the contact stiffness ($k_C = 100$ MN/m), superposed upon both the Lyapunov spectra and the resonant frequency response. Two different diagrams are of concern. The upper part presents the maximum values for up-sweep and down-sweep simulations, showing the resonant conditions and dynamical jumps. On the other hand, lower diagram considers Poincaré sections, identifying the bifurcations. The dot-dash lines (at $k_C = 100$ MN/m in Fig. 7a and at $\Omega = 130$ rad/s in Fig. 7b) correspond to the case analyzed in Fig. 6. These results confirm the chaotic behavior for these parameter values. Note that dynamical jumps are found either near the dashed boundaries or at crisis breakpoints due to an abrupt change in the dynamical behavior in both cases.

It is noticeable from Fig. 7a that the increase in the contact stiffness k_C for an intermittent contact region, is related to a periodic behavior up to approximately 50 MN/m. Then, for higher values of k_C, a predominant chaotic behavior occurs, except for some periodic windows identified for all negative Lyapunov exponents' values, which subtitles are the same adopted for λ_i ($i = 1, 2, 3, ..., 8$) in Fig. 6g. In Fig. 7b, the dashed lines indicate the transition boundaries between permanent and intermittent contact regions, according to Fig. 5b. The beginning and finishing ranges of x_s-null displacement correspond to non-contact regions. In the leftward intermittent contact region ($130 < \Omega < 140$ rad/s, approximately), periodic (mostly, period-1) and chaotic responses occur. In the full contact region ($140 < \Omega < 160$ rad/s, approximately), period-1 solution prevails, migrating to a chaotic behavior in the rightward intermittent contact region ($160 < \Omega < 165$ rad/s, approximately). Near the right boundary from full to intermittent contact region near $\Omega = 160$ rad/s, a quasi-periodic behavior takes place. This feature may be inferred through the higher Lyapunov exponent λ_1 crossing the null value from negative to positive, together with slight scattered points in the bifurcation diagram near this boundary.

Figure 8 presents new basins of attraction concerning the same parameter space of Fig. 4 ($\Omega \times k_C$), again varying the friction coefficient from $\mu = 0$ up to $\mu = 0.3$, but this time, mapping the kind of dynamical
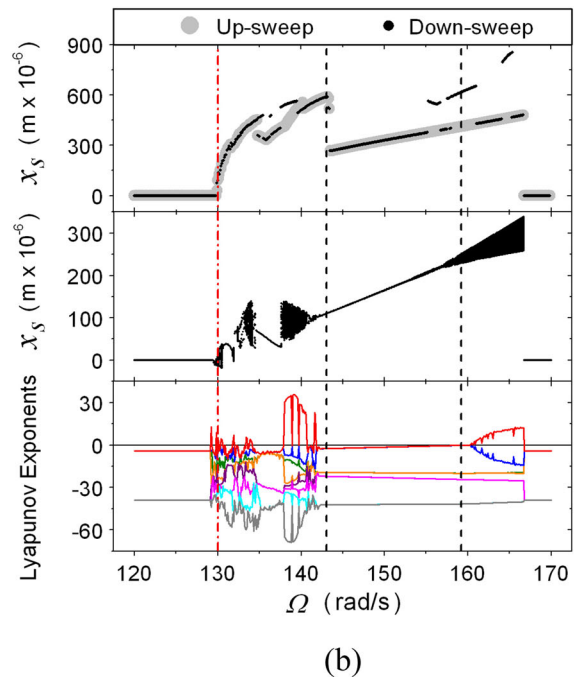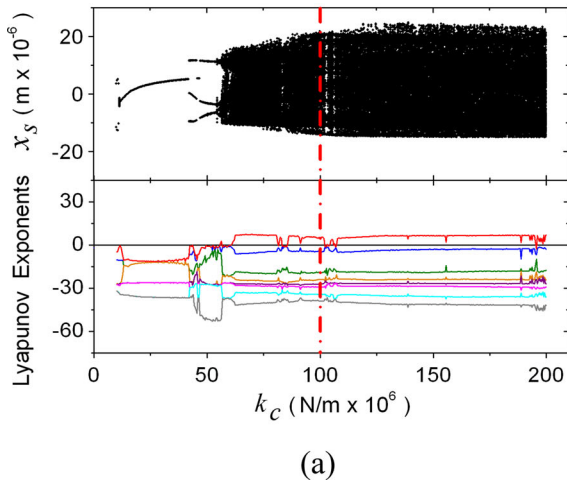
(a)

(b)

Fig. 7 Dynamical analysis considering the routes set in Fig. 5b for $\mu = 0.1$. **a** Bifurcation diagram and Lyapunov exponents varying k_C with fixed $\Omega = 130$ rad/s (vertical route of Fig. 5b);

b Resonant frequency response, bifurcation diagram and Lyapunov exponents varying Ω with fixed $k_C = 100$ MN/m (horizontal route of Fig. 5b)

pattern (periodic, chaotic, hyperchaotic). In the upcoming results, the frequency range is restricted to the full/intermittent region of the contact nature maps presented in Fig. 4: from $\Omega = 130$ rad/s to $\Omega = 165$ rad/s—which is the actual range of interest. The solid black lines represent the transition boundaries between full and intermittent contact regions, according to Fig. 4, while dashed lines are used to indicate the eroded boundary. Each parameter space contains 35.024 mesh points (176 points for Ω *versus* 199 points for k_C). For a null friction coefficient condition (Fig. 8a, for $\mu = 0$), there are two distinct regions: a predominant period-1 region rightward from the linearized natural frequency ($\Omega = 140$ rad/s), related to a full contact condition; while, leftward from this frequency, a messy colored intermittent contact region takes place, with nearly vertical stripes of different dynamical behaviors, including a blurry hyperchaotic one. Since a non-null friction coefficient is adopted (Fig. 8b, for $\mu = 0.095$), an intermittent contact zone arises in the northeastern region of the parameters space, presenting a chaotic behavior near the upper right corner of the basin. Besides that, in the left intermittent contact region, the former messy

colored region loses complexity and a thick period-1 vertical stripe emerges. With the friction coefficient increment (Fig. 8c, d), the northeastern intermittent contact zone increases and the accompanying chaotic region increases as well, approaching the left transition boundary at the linearized natural frequency ($\Omega = 140$ rad/s). For higher friction coefficient values (Fig. 8e, f and g), the left and right transition boundary merges, such that the rightward growing chaotic region meets the vertical chaotic stripe around the linearized natural frequency. For even higher friction coefficient values (Fig. 8h, i), complex dynamical behaviors spread out over almost the whole basin, with a pronounced hyperchaotic region rightward from the linearized natural frequency.

In the sequel, the preeminence of each one of the dynamical patterns classified for different friction coefficients is considered. Figure 9 shows that for low friction coefficient values (from $\mu = 0$ up to $\mu = 0.105$), a period-1 response is predominant. Nevertheless, when the northeastern intermittent contact zone, associated with chaotic behavior, starts to increase significantly (from $\mu = 0.95$ on), the period-1 response starts to decrease. For $\mu \cong 0.11$, these two
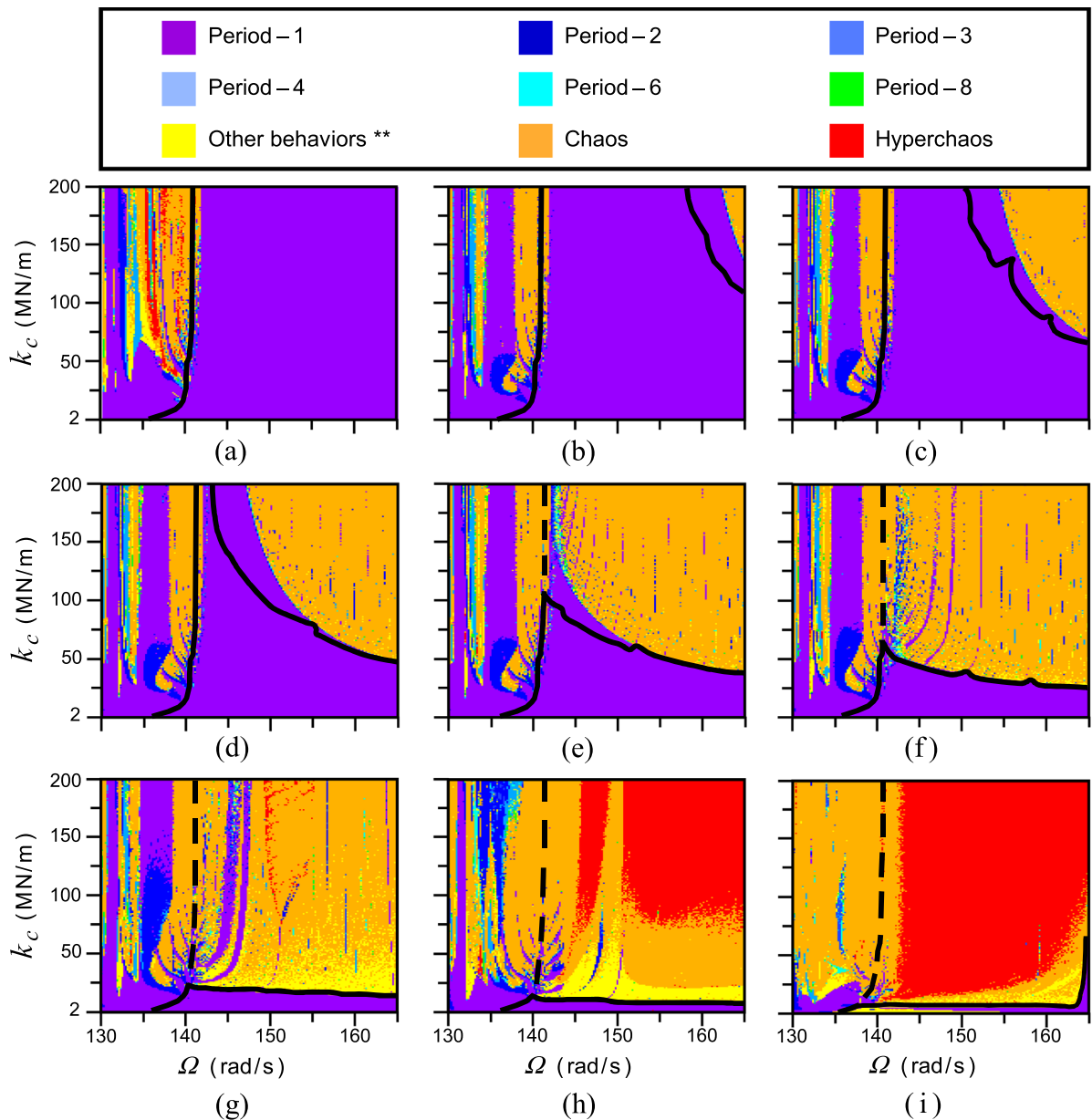
Fig. 8 Basin of attraction mapping the dynamical pattern evolution varying the friction coefficient. **a** $\mu = 0$; **b** $\mu = 0.095$; **c** $\mu = 0.100$; **d** $\mu = 0.105$; **e** $\mu = 0.110$; **f** $\mu = 0.120$; **g** $\mu = 0.150$; **h** $\mu = 0.200$; **i** $\mu = 0.300$. **The classification "other behaviors" refer to: period-5, period-7, higher periodicities (more than 8) and quasi-periodicity

behaviors share nearly equal proportions, summing almost 100% of the basin. When $\mu = 0.12$, the chaotic behavior reaches its maximum (around 60%), while period-1 behavior continues to decrease. From $\mu = 0.12$ on, scape region related to "other behaviors" starts to increase more significantly, reaching a maximum around 10% for $\mu = 0.15$ and reducing the

chaotic fraction. From $\mu = 0.15$ on, the occurrence of hyperchaotic behavior drastically increases, reducing all other dynamical patterns, including the chaotic one. All other behaviors (other than those discussed) do not reach 10%. Among them, only period-2 behavior deserves some attention, presenting 5 to 6%, for
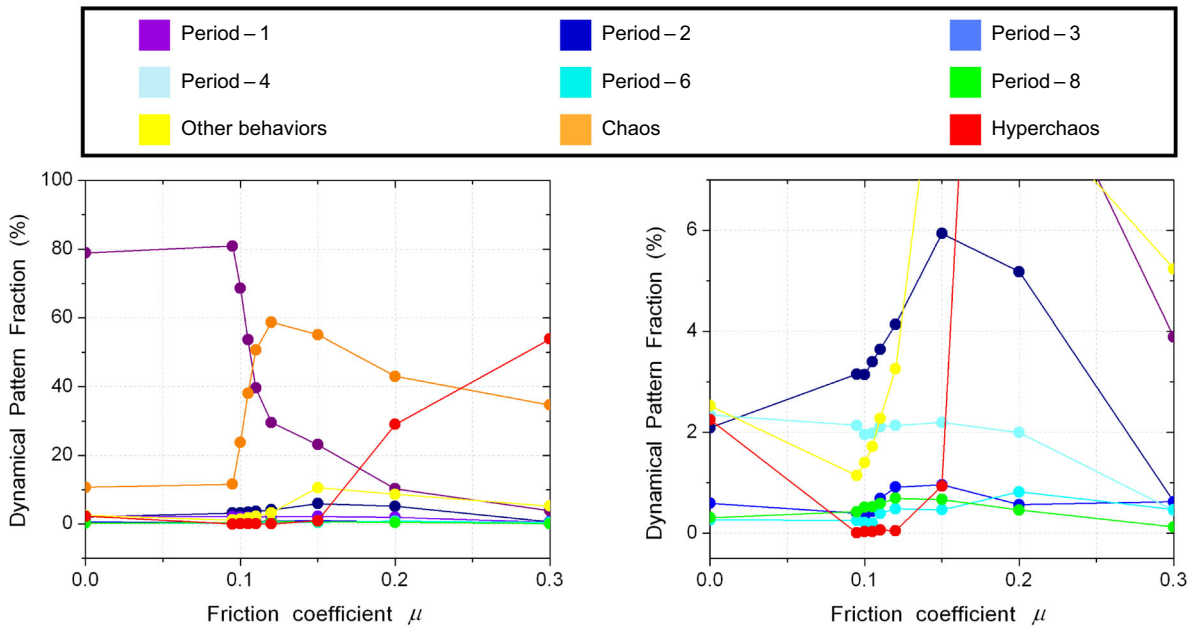
Fig. 9 Dynamical pattern fraction as a function of the friction coefficient μ. **a** Full range; **b** detail to highlight low values
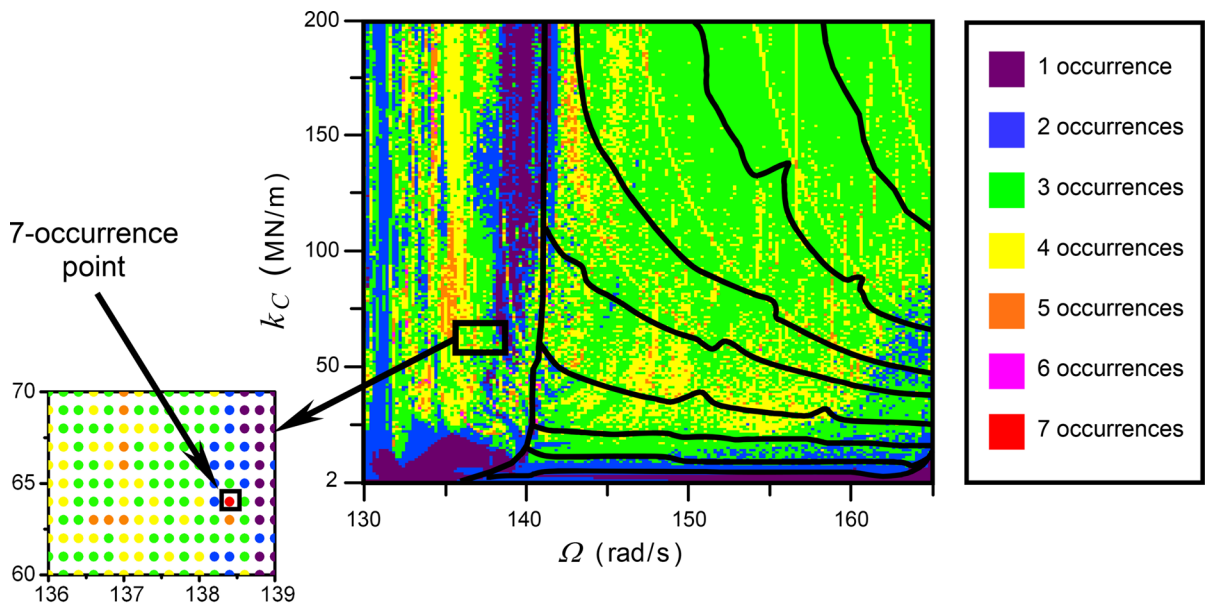

Fig. 10 Basin of attraction mapping the dynamical pattern variation through the variation of friction coefficient

intermediate friction coefficient values ($0.15 < \mu < 0.2$).

Figure 10 considers the same parameter space ($\Omega \times k_C$) of the preceding analyses, but computing how many times each mesh point changes its dynamical pattern, while the friction coefficient varies from $\mu = 0$ up to $\mu = 0.3$ (discretization assumes 9 variations through this range). The legend colors represent the number of different dynamical patterns (occurrences) each mesh point assumes. The solid black lines represent the transition boundaries evolution between full and intermittent contact regions, while μ varies.

It is not an easy task to interpret the whole parameter space; though, specific regions discussed during Fig. 8 analysis allow some conclusions. With this purpose, the next analysis is conducted for two distinct regions: the left intermittent region and the right region that undergoes erosion.

In the left intermittent region, the structure with vertical stripes identified in Fig. 8 shows up again, as follows: around $\Omega = 130$ rad/s, a thin messy colored vertical stripe indicates several occurrences; right after that, there is a thin 2-occurrence stripe that is associated with the transition from the period-1 stripe observed in Fig. 8a up to Fig. 8h to chaotic behavior present in Fig. 8i; around $\Omega = 135$ rad/s, a thick messy colored vertical stripe indicates several occurrences again. This region goes through several changes, during the friction coefficient evolution presented in Fig. 8; before $\Omega = 140$ rad/s, a mainly 1-occurrence stripe is associated with chaotic behavior near the rotor natural frequency; for low contact stiffness values ($k_C < 25$ MN/m), an 1-occurrence region is related to a period-1 response.

Concerning the right region that undergoes erosion, it is possible to identify a kind of a predominant 3-occurrence matrix with some 4-occurrence lamellas. This 3-occurrence matrix is associated with the transition from period-1 response of the original permanent contact region to the chaotic response of the new intermittent contact region (after basin erosion) that, eventually, gives rise to a hyperchaotic behavior for high friction coefficients ($\mu > 0.15$). For intermediate contact stiffness values ($k_C < 50$ MN/m), in this 3-occurrence matrix, the hyperchaotic behavior is substituted for an "other behaviors" response. The well-defined 4-occurrence lamellas may be associated with the thin slice containing different periodic behaviors that limits the growing chaotic zone boundaries, which arises together with the intermittent contact region. Near the rotor natural frequency, for high contact stiffness values (k_C around 150 MN/m), these lamellas turn into sprayed 5-occurrence ones. The 2-ccurrence points (always near the transition boundaries) experiment a single transition: from period-1 (full contact) to either chaotic response or "other behaviors" response (intermittent contact). At last, the remaining permanent contact region (for $\mu = 0.3$) is mainly associated with a period-1 response.

Figure 11 quantifies the absolute amount of mesh points and the respective percentage for each number
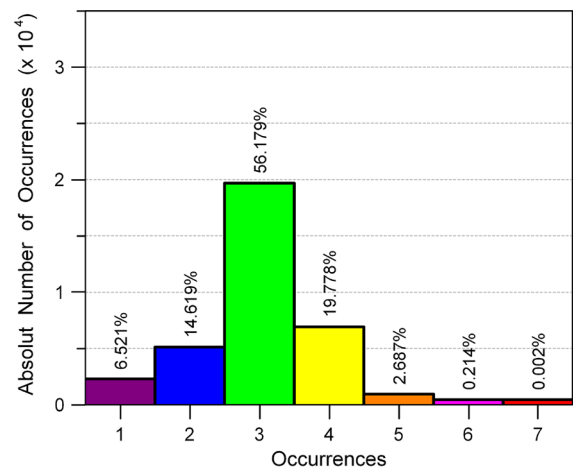

Fig. 11 Dynamical pattern variation based on the occurrence analysis

of occurrences for the parameter space of Fig. 10. Note that there are more 3-occurrence points, followed by 4-occurrence points, 2-occurrence points and 1-occurrence points. Other numbers of occurrences are almost negligible. An interesting issue is that the greatest number of occurrences (7 occurrences) only happens for 1 point in the whole mesh. This point is assigned in the depicted detail of Fig. 10 and takes place for $\Omega = 138.4$ rad/s and $k_C = 64$ MN/m.

Figure 12 considers the dynamical behaviors related to these specific values of Ω and k_C for the nine friction coefficient values ($\mu = 0$ up to $\mu = 0.3$) covered during the previous parameter space analysis, showing that, in fact, seven different dynamical patterns occur. Results comprise stator orbits for the x-direction with their Poincare sections in the state subspace $x_s \times \dot{x}_s$ and the respective Lyapunov exponents' spectra, following the same definition adopted for λ_i ($i = 1, 2, 3, ..., 8$) in Fig. 6g. The depicted details of state subspaces help to identify the behaviors' periodicity, while depicted details of Lyapunov spectra settle possible doubts about near-zero exponents. Figure 12a shows ($\mu = 0$) that there are tangle trajectories in the state subspace with a strange attractor in the Poincare section. A single positive Lyapunov exponent attests the chaotic behavior. Figure 12b ($\mu = 0.095$) shows similar results compared to those obtained in Fig. 12a. Again, a single positive Lyapunov exponent attests the chaotic behavior. In Fig. 12c ($\mu = 0.1$), a closed orbit suggests a periodic behavior and the depicted Poincare section

(a)   (b)   (c)

(d)   (e)   (f)

(g)   (h)   (i)
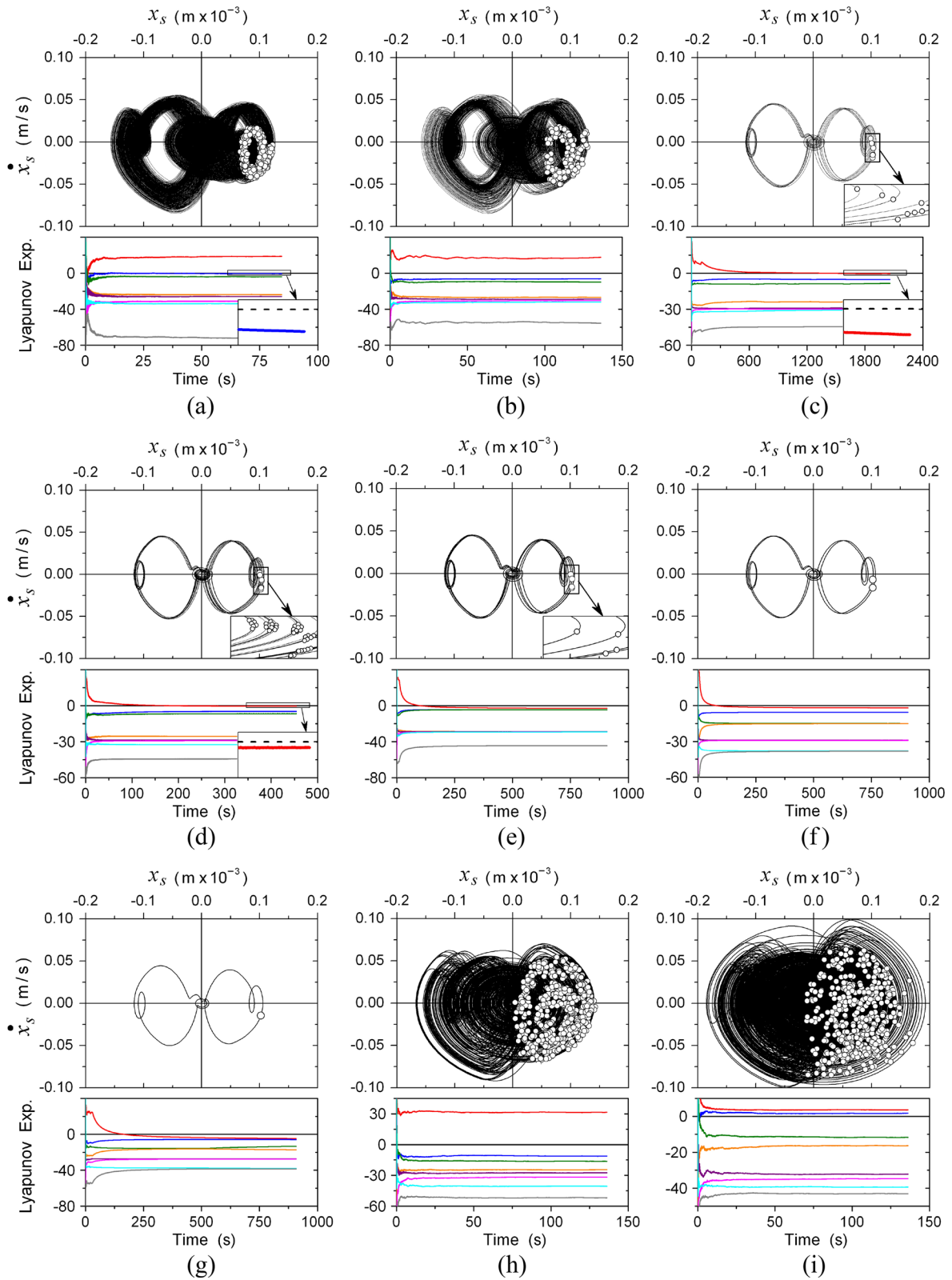
◄ **Fig. 12** Stator trajectories and respective Lyapunov exponents'
spectra with fixed $\Omega = 138.4$ rad/s and $k_C = 64$ MN/m, varying
the friction coefficient. **a** $\mu = 0$; **b** $\mu = 0.095$; **c** $\mu = 0.100$;
d $\mu = 0.105$; **e** $\mu = 0.110$; **f** $\mu = 0.120$; **g** $\mu = 0.150$; **h** μ 0.200;
i $\mu = 0.300$

reveals a period-8 response. All negative Lyapunov
exponents ensure the periodic behavior. Figure 12d
($\mu = 0.105$) shows an apparent closed orbit, but the
zoom in the depicted detail reveals a slight shift in the
trajectories for different cycles, suggesting a quasi-
periodic behavior. The zoom in the Poincare section
provides several close points, confirming this insight.
The higher Lyapunov exponent tending to zero in the
depicted detail also attests the quasi-periodic behavior.
Figure 12e ($\mu = 0.11$) shows a closed orbit that
indicates a periodic behavior, and the Poincare section
reveals a period-4 response. All negative Lyapunov
exponents ensure the periodic behavior. Figure 12f
($\mu = 0.12$) and Fig. 12g ($\mu = 0.15$) show periodic
behaviors as well; however, this time, period-2 and
period-1 behaviors take place, respectively, both with
negative Lyapunov exponents. Figure 12h ($\mu = 0.2$)
tangle trajectories reappear in the state subspace and
the Poincare section still preserves some lamellar
structure characterizing a strange attractor. The single
positive Lyapunov exponent attests this chaotic
behavior. Figure 12i ($\mu = 0.3$) the tangle trajectories
remain in the state subspace presenting a Poincare
section characterized by a collection of points with no
apparent structure, which is a hyperchaotic character-
istic. Two positive Lyapunov exponents ratify the
hyperchaotic behavior.

4 Concluding remarks

This paper presents a numerical investigation of the
nonlinear dynamics of a four-degree of freedom
Jeffcott rotor–stator, considering nonsmooth impact
between them. The stator inner coating surface
propitiates elastic restitution (normal impact) and
Coulomb friction (tangential rubbing). A multipara-
metric analysis shows different parameter spaces,
varying rotating speed, contact stiffness and friction
coefficient. Based on the contact between rotor and
stator, the contact nature is classified into three
dynamical modes: no contact, intermittent contact or

full contact. After that, parameter spaces classify the
dynamical response into periodic (considering differ-
ent periodicities) or chaotic/hyperchaotic. At last, a
parameter space accounts for dynamical pattern
changes as a function of the friction coefficient.

During the contact nature analysis, for a no friction
condition, the contact stiffness revealed no influence;
however, while varying the rotating speed, there are no
contact regions for low and high values (compared to
the rotor-alone natural frequency) and an intermediate
frequency range around this natural frequency where
near leftward from it, an intermittent contact region
takes place; and rightward from it, a full contact region
occurs. While increasing the friction coefficient, the
only region affected is the full permanent contact
region that undergoes an erosion, giving rise to an
intermittent contact region. It is possible to infer that,
lower values of contact stiffness (which implies low
values of tangential contact force, which means
friction), inhibit intermittent contact behavior, while
increasing the friction coefficient.

Regarding the dynamical response, intermittent
contact condition is the most interesting one, present-
ing rich and complex behaviors. Within the full
contact region, period-1 behavior prevails; besides
that, low contact stiffness values also present period-1
behavior. During the full contact region erosion, the
growing nucleated intermittent contact region always
presents complex behavior, migrating from chaotic to
hyperchaotic (for high values of friction coefficient).
Moreover, chaotic behavior is found near the rotor-
alone natural frequency, regardless of the friction
coefficient. Undoubtedly, the increase in the friction
coefficient turns the system response more complex.

The parameter space concerning the dynamical
pattern change clearly shows that the intermittent
contact region leftward from the rotor-alone natural
frequency is the richest zone, undergoing several
changes while varying the friction coefficient. The full
contact eroded region presents a main 3-occurence
response, migrating from period-1 (for a no friction
condition and full contact) to chaos (for intermediate
values of friction coefficient and intermittent contact),
ending up hyperchaotic (for high values of friction
coefficient still with intermittent contact). A 1-occur-
rence lamella near the rotor-alone natural frequency
attests the chaotic behavior, regardless of the friction
coefficient.

Data availability The datasets generated during and/or analyzed during the current study are available from the corresponding author on reasonable request.

Declarations

Conflict of interest The authors declare that they have no conflict of interest.

References

1. Ahmad, S.: Rotor casing contact phenomenon in rotor dynamics-literature survey. J. Vib. Control **16**(9), 1369–1377 (2010)
2. Al-Bedoor, B.O.: Transient torsional and lateral vibrations of unbalanced rotors with rotor-to-stator rubbing. J. Sound Vib. **229**, 627–645 (2000)
3. Ali Hajnayeb, R.B., Sedighi, H.M.: Comments on: nonlinear phenomena, bifurcations, and routes to chaos in an asymmetrically supported rotor-stator contact system, by Philip Varney and Yitzhak green. J. Sound Vib. **409**, 336–342 (2017)
4. Alves, M.T.S., Steffen, V., Jr., Santos, M.C., Savi, M.A., Enemark, S., Santos, I.F.: Vibration control of a flexible rotor suspended by shape memory alloy wires. J. Intell. Mater. Syst. Struct. **29**(11), 2309–2323 (2018)
5. Behzad, M., Alvandi, M.: Unbalance-induced Rub between rotor and compliant-segmented stator. J. Sound Vib. **429**, 96–129 (2018)
6. Boyaci, A.: Numerical continuation applied to nonlinear rotor dynamics. Procedia IUTAM **19**, 255–265 (2016)
7. Brandão, A., Paula, A.S., Savi, M.A., Thouverez, F.: Nonlinear dynamics and chaos of a nonsmooth rotor-stator system. Math. Probl. Eng. **10**, 1523 (2017)
8. Chasalevris, A.: Stability and Hopf bifurcations in rotor-bearing-foundation systems of turbines and generators. Tribol. Int. **145**, 106154 (2020)
9. Chávez, J.P., Hamaneh, V.V., Wiercigroch, M.: Modelling and experimental verification of an asymmetric Jeffcott rotor with radial clearance. J. Sound Vib. **334**, 86–97 (2015)
10. Chávez, J.P., Wiercigroch, M.: Bifurcation analysis of periodic orbits of a non-smooth jeffcott rotor model. Commun. Nonlinear Sci. Numer. Simul. **18**, 2571–2580 (2013)
11. Chipato, E., Shaw, A.D., Friswell, M.I.: Frictional effects on the nonlinear dynamics of an overhung rotor. Commun. Nonlinear Sci. Numer. Simul. **78**, 104875 (2019)
12. Choy, F.K., Padovan, J.: Non-linear transient analysis of rotor-casing rub events. J. Sound Vib. **113**, 529–545 (1987)
13. Divenyi, S., Savi, M.A., Franca, L.F.P., Weber, H.I.: Nonlinear dynamics and chaos in systems with discontinuous support. Shock. Vib. **13**(4/5), 315–326 (2006)

14. Edwards, S., Lees, A.W., Friswell, M.I.: The influence of torsion on rotor/stator contact in rotating machinery. J. Sound Vib. **225**, 767–778 (1999)
15. Ehehalt, U., Alber, O., Markert, R., Wegener, G.: Experimental observations on rotor-to-stator contact. J. Sound Vib. **446**, 453–467 (2019)
16. El-Sayed, T.A., Sayed, H.: Bifurcation analysis of rotor/bearing system using third-order journal bearing stiffness and damping coefficients. Nonlinear Dyn. **107**, 123–151 (2022)
17. Fonseca, C.A.L.L., Aguiar, R.R., Weber, H.I.: On the nonlinear behaviour and orbit patterns of rotor/stator contact with a non-conventional containment bearing. Int. J. Mech. Sci. **105**, 117–125 (2016)
18. Fonseca, C.A.L.L., Santos, I.F., Weber, H.I.: An experimental and theoretical approach of a pinned and a conventional ball bearing for active magnetic bearings. Mech. Syst. Signal Process. **138**, 17 (2020)
19. He, Y., Oi, S., Chu, F., Li, H.: Vibration control of a rotor-bearing system using shape memory alloy: I. Theory Smart Mater. Struct. **16**, 114–121 (2007)
20. He, Y., Oi, S., Chu, F., Li, H.: Vibration control of a rotor-bearing system using shape memory alloy: II. Experim. Study Smart Mater. Struct. **16**, 122–127 (2007)
21. Ishida, Y., Yamamoto, T.: Linear and Nonlinear Rotordynamics. Wiley, Haboken (2012)
22. Lahriri, S., Santos, I.: Theoretical modelling, analysis and validation of the shaft motion and dynamic forces during rotor-stator contact. J. Sound Vib. **332**, 6359–6376 (2013)
23. Kapitaniak, M., Vaziri, V., Chávez, J.P., Wiercigroch, M.: Experimental studies of forward and backward whirls of drill-string. Mech. Syst. Signal Process. **100**, 454–465 (2018)
24. Kramer, E.: Dynamics of Rotors and Foundations. Springer, New York (1993)
25. Leine, R.I., van Campen, D.H., van de Vrande, B.L.: Bifurcations in nonlinear discontinuous systems. Nonlinear Dyn. **23**, 105–164 (2000)
26. Mokhtar, M.A., Darpe, A.K., Gupta, K.: Investigation of Rotor Stator Rub Phenomenon Considering Pure Sticking Condition. Procedia Eng. **173**, 1531–1537 (2017)
27. Moreira, R.V. and Paiva, A.: The Influence of Friction in Rotor–Stator Contact Nonlinear Dynamics. in Proceedings of the 10th International Conference on Rotor Dynamics—IFToMM 2018 in Mechanisms and Machine Science. Springer International Publication, pp. 428–441, (2019)
28. Muszynska, A.: Rotordynamics. Taylor & Francis Group, New York (2005)
29. Muszynska, A., Goldman, P.: Chaotic responses of unbalanced rotor/bearing/stator systems with looseness or rubs. Chaos, Solitons Fract. **5**, 1683–1704 (1995)
30. Nguyen, K.L., Tran, Q.T., Andrianoely, M.A., Manin, L., Baguet, S., Dufour, R., Mahjoub, M., Menand, S.: Nonlinear rotordynamics of a drillstring in curved wells: models and numerical techniques. Int. J. Mech. Sci. **166**, 105225 (2020)
31. Popprath, S., Ecker, H.: Nonlinear dynamics of a rotor contacting an elastically suspended stator. J. Sound Vib. **308**, 767–784 (2007)
32. Rahman, M.A., Siddique, S.M.M., Rahman, M.M.: Whirling of a jeffcott rotor on a superelastic sma shaft. AIP Conf.

Proc. **2324**, 030027 (2021). https://doi.org/10.1063/5.0037615

33. Saint Martin, L.B., Mendes, R.U., Cavalca, K.L.: Model reduction and dynamic matrices extraction from state-space representation applied to rotating machines. Mech. Mach. Theory **149**, 103804 (2020)

34. Savi, M.A., Divenyi, S., Franca, L.F.P., Weber, H.I.: Numerical and experimental investigations of the nonlinear dynamics and chaos in non-smooth systems. J. Sound Vib. **301**(1–2), 59–73 (2007)

35. Silva, L.C., Savi, M.A., Paiva, A.: Nonlinear dynamics of a rotordynamic nonsmooth shape memory alloy system. J. Sound Vib. **332**, 608–621 (2013)

36. Srinivas, R.S., Tiwari, R., Kannababu, Ch.: Application of active magnetic bearings in fexible rotordynamic systems—a state-of-the-art review. Mech. Syst. Signal Process. **106**, 537–572 (2018)

37. Tiwari, R.: Rotor Systems: Analysis and Identification. Taylor & Francis Group, New York (2018)

38. Tuckmantel, F.W.S., Cavalca, K.L.: Vibration signatures of a rotor-coupling-bearing system under angular misalignment. Mech. Mach. Theory **133**, 559–583 (2019)

39. Varney, P., Green, I.: Nonlinear phenomena, bifurcations, and routes to chaos in an asymmetrically supported rotor-stator contact system. J. Sound Vib. **336**, 207–226 (2015)

40. Vlajic, N., Champneys, A.R., Balachandran, B.: Nonlinear dynamics of a jeffcott rotor with torsional deformations and rotor-stator contact. Int. J. Non-Linear Mech. **92**, 102–110 (2017)

41. Wang, H.: Passive vibration reduction of a squeeze film damper for a rotor system with fit looseness between outer ring and housing. J. Low Freq. Noise Vib. Active Control **40**(3), 1473–1492 (2021)

42. Xie, D., Huang, Z., Ma, Y., Vaziri, V., Kapitaniak, M., Wiercigroch, M.: Nonlinear dynamics of lump mass model of drill-string in horizontal well. Int. J. Mech. Sci. **174**, 14 (2020)

43. Yang, Y., Tang, J., Chen, G., Yang, Y., Cao, D.: Rub-impact investigation of a single-rotor system considering coating effect and coating hardness. J. Vib. Eng. Technol. (2020). https://doi.org/10.1007/s42417-020-00243-0

44. Yao, J., Liu, L., Yang, F., Scarpa, F., Gao, J.: Identification and optimization of unbalance parameters in rotor-bearing systems. J. Sound Vib. **431**, 54–69 (2018)

45. Zhang, H., Lu, K., Zhang, W., Fu, C.: Investigation on dynamic behaviors of rotor system with looseness and nonlinear supporting. Mech. Syst. Signal Process. (2022). https://doi.org/10.1016/j.ymssp.2021.108400